

L

LAND SURFACE EMISSIVITY

Alan Gillespie
Department of Earth and Space Sciences, University
of Washington, Seattle, WA, USA

Definitions

Land surface emissivity (LSE). Average emissivity of an element of the surface of the Earth calculated from measured radiance and land surface temperature (LST) (for a complete definition, see Norman and Becker, 1995).

Atmospheric window. A spectral wavelength region in which the atmosphere is nearly transparent, separated by wavelengths at which atmospheric gases absorb radiation. The three pertinent regions are “visible/near-infrared” ($\sim 0.4\text{--}2.5\ \mu\text{m}$), mid-wave infrared ($\sim 3\text{--}5\ \mu\text{m}$) and long-wave infrared ($\sim 8\text{--}14\ \mu\text{m}$).

Blackbody. An ideal material absorbing all incident energy or emitting all thermal energy possible. A cavity with a pinhole aperture approximates a blackbody.

Brightness temperature. The temperature of a blackbody that would give the radiance measured for a surface.

Color temperature. Temperature satisfying Planck’s law for spectral radiances measured at two different wavelengths.

Contrast stretch. Mathematical transform that adjusts the way in which acquired radiance data translate to the black/white dynamic range of the display monitor.

Emissivity ϵ . The efficiency with which a surface radiates its thermal energy.

Irradiance. The power incident on a unit area, integrated over all directions (W m^{-2}).

Graybody. A material having constant but non-unity emissivity.

Long-wave infrared (LWIR). For most terrestrial surfaces ($\sim 340\ \text{K}$ to $\sim 240\ \text{K}$), peak thermal emittance occurs in the LWIR ($\sim 8\text{--}14\ \mu\text{m}$).

Mid-infrared (MIR). Forest fires ($\sim 1,000\text{--}600\ \text{K}$) have peak thermal emittances in the MIR ($\sim 3\text{--}5\ \mu\text{m}$).

Noise equivalent Δ temperature (NE Δ T). Random measurement error in radiance propagated through Planck’s law to give the equivalent uncertainty in temperature.

Path radiance S_{\uparrow} . The power per unit area incident on a detector and emitted upward from within the atmosphere ($\text{W m}^{-2}\ \text{sr}^{-1}$).

Planck’s law. A mathematical expression relating spectral radiance emitted from an ideal surface to its temperature (Equation 1, in the entry *Land Surface Temperature*).

Radiance. The power per unit area from a surface directed toward a sensor, in units of $\text{W m}^{-2}\ \text{sr}^{-1}$.

Reflectivity ρ . The efficiency with which a surface reflects energy incident on it.

Reststrahlen bands. Spectral bands in which there is a broad minimum of emissivity associated in silica minerals with interatomic stretching vibrations of Si and O bound in the crystal lattice.

SEBASS. Spatially Enhanced Broadband Array Spectrograph System, a hyperspectral TIR imager (Hackwell et al., 1996).

Short-wave infrared (SWIR). Erupting basaltic lavas ($\sim 1,400\ \text{K}$) have their maximum thermal emittance at $\sim 2.1\ \mu\text{m}$ in an atmospheric window at $0.4\text{--}2.5\ \mu\text{m}$. Part of this spectral region ($1.4\text{--}2.5\ \mu\text{m}$) is called the SWIR.

Sky irradiance I_{\downarrow} . The irradiance on the Earth’s surface originating as thermal energy radiated downward by the atmosphere (W m^{-2}) (spectral irradiance: $\text{W m}^{-2}\ \mu\text{m}^{-1}$).

Spectral radiance L . Radiance per wavelength, in units of $\text{W m}^{-2}\ \mu\text{m}^{-1}\ \text{sr}^{-1}$.

Thermal infrared (TIR). Thermal energy is radiated from a body at frequencies or wavelengths in proportion to its temperature. The wavelengths for which this radiant energy

is significant for most terrestrial surfaces ($\sim 1.4\text{--}14\ \mu\text{m}$) are longer than the wavelength of visible red light and hence are known as thermal infrared. The TIR is subdivided into three ranges (LWIR, MIR, SWIR) for which the atmosphere is transparent (atmospheric “windows”) so that the energy can be measured from space.

Introduction

Thermal emissivity ε is the efficiency with which a surface emits its stored heat as thermal infrared (TIR) radiation. It is useful to know because it indicates the composition of the radiating surface and because it is necessary as a control in atmospheric and energy-balance models, since it must be known along with brightness temperature to establish the heat content of the surface. The first practical demonstration of multispectral TIR imaging for compositional mapping was from a NASA airborne scanner flown over Utah (Kahle and Rowan, 1980).

Emissivity differs from wavelength to wavelength, just as reflectivity ρ does in the spectral region of reflected sunlight ($0.4\text{--}2.5\ \mu\text{m}$). Emissivity is defined as

$$\varepsilon(\lambda) = \frac{L(\lambda, T)}{B(\lambda, T)} \quad (1)$$

where L is the measured spectral radiance and B is the theoretical blackbody spectral radiance for a surface with a skin temperature T . B is given by Planck’s law which, together with the basic physics of TIR radiative transfer, is discussed in the entry *Land Surface Temperature* (LST).

Unlike T , which is a variable property of a surface controlled by the heating history and not directly by composition, $\varepsilon(\lambda)$ is independent of T and is a function directly of composition. Furthermore, $\varepsilon(\lambda)$ in the TIR wavelengths ($3\text{--}14\ \mu\text{m}$) responds to different aspects of composition than reflectivity $\rho(\lambda)$ at $0.4\text{--}2.5\ \mu\text{m}$. In general, ρ at wavelengths $0.4\text{--}2.5\ \mu\text{m}$ is controlled by the amounts of iron oxides, chlorophyll, and water on the surface; ε in the TIR is controlled more by the bond length of Si and O in silicate minerals. Examples of emissivity spectra are given in Figure 1.

TIR spectroscopy is especially important because silicate minerals are the building blocks of the geologic surface of Earth, and their presence and amounts can be inferred only indirectly at shorter wavelengths. Thus TIR spectroscopy is complementary to spectroscopy of reflected sunlight. Good summaries of TIR spectroscopy and its significance in terms of surface composition may be found in Lyon (1965), Hunt (1980), and Salisbury and D’Aria (1992). A good introduction to spectral analysis may be found in Clark et al. (2003).

Figure 1 shows daytime and nighttime false-color composite images of spectral radiance from a sparsely vegetated part of Death Valley, California, enhanced using a decorrelation contrast stretch (Soha and Schwartz, 1978; Gillespie et al., 1986). This stretch emphasizes the emissivity component of the signal, shown as color, and

de-emphasizes the temperature, shown as dark/light intensity. In addition to composition, the daytime image gives a good sense of topography, because sunlit slopes are warmer than shadowed slopes. In the nighttime image, most temperature effects are subdued, and the image closely resembles the Land Surface Emissivity (LSE) alone.

Exceptions include standing water, which is cooler than the land during the day but warmer at night. Standing water (C) in the floor of Death Valley shows dark green in the daytime image but light pink in the nighttime image. Vegetation (A) appears dark in the daytime image, when it is cooling its canopy by evapotranspiration. The toe of an alluvial fan (B) appears darker at night, when soil moisture rises to the surface and evaporates.

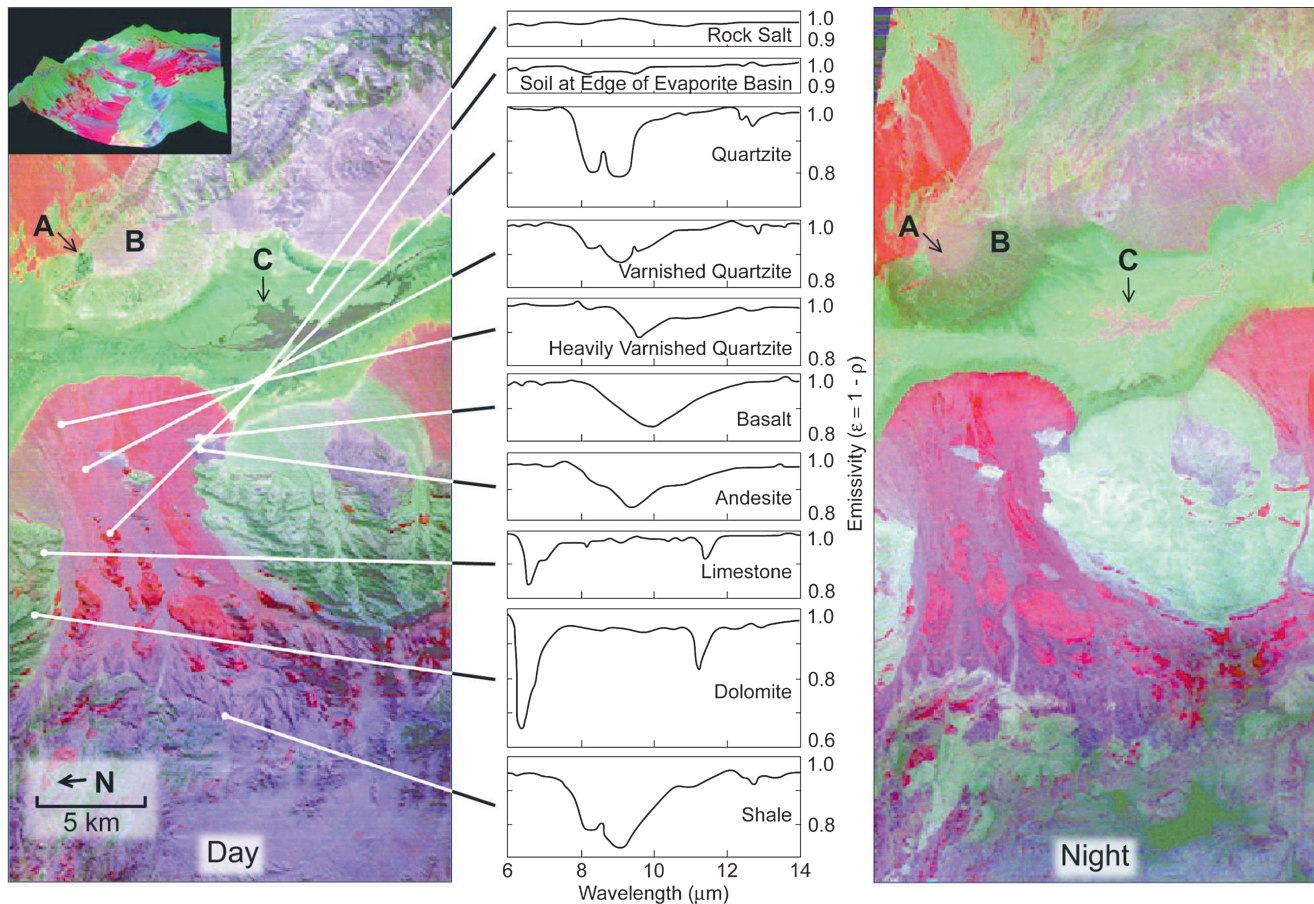
The colors in Figure 1 indicate rock type. For example, the emissivity of quartzite is low (~ 0.8) at 8.3 and $9.1\ \mu\text{m}$ (blue and green) but high at $10.4\ \mu\text{m}$ (red); therefore, it is displayed as red. Other rock types and display colors can be understood by comparing the images and emissivity spectra in Figure 1.

The discussion below focuses on algorithms designed to recover emissivities from remotely sensed spectral radiance data. Figure 2, of a desert landscape, compares spectral radiance to temperature and emissivity images recovered from it. Also shown are emissivity spectra of vegetation and the geologic substrate. As explained in the entry *Land Surface Temperature*, temperature and emissivity recovery is an underdetermined problem, and dozens of approaches have been proposed and published that break down the indeterminacy. These fall in four classes: deterministic algorithms that solve for *LST* and *LSE* exactly, algorithms that recover the shape of the LSE spectrum only, model approaches that make key assumptions, and algorithms that attempt also to scale or calibrate the normalized spectra to their actual emissivity values.

In evaluating the algorithms, it is useful to ask how accurately it is necessary to recover LSE and LST. For example, many analytic algorithms that seek to identify surface composition rely not so much on actual emissivity values, but on the central wavelengths of emissivity minima (e.g., reststrahlen bands), which can be diagnostic for many rocks and minerals. If this is your goal, it may not be necessary to scale the spectra, relying instead on the simpler algorithms that just recover spectral shape.

Errors in LST may affect some algorithms by warping the spectra over several μm of wavelength. This happens because the shape of the Planck function changes with temperature (*Land Surface Temperature*, Figure 2). A 5 K error at 300 K, for example, will cause a slope in the recovered emissivity spectrum of 0.05 from 8 to 14 μm . However, the sharp mineralogical features ($\sim 0.2\text{--}0.5\ \mu\text{m}$ wide) are readily distinguished against this distorted continuum.

The TIR is commonly a difficult spectral region in which to measure spectral radiance, and the images are typified by a low signal–noise ratio. This ratio is commonly represented by the “noise equivalent Δ temperature” or



Land Surface Emissivity, Figure 1 Airborne thermal infrared multispectral scanner (TIMS: Palluconi and Meeks, 1985) false-color TIR radiance images of Death Valley, California (RGB = 10.4, 9.1, 8.3 μm). Letters A, B, and C indicate sites discussed in the text. *Central column* shows laboratory spectra for field samples. *Inset* shows similar ASTER image “draped” over topography, looking north up Death Valley. The TIMS images cross the central part of the ASTER footprint (Courtesy Harold Lang and Anne Kahle, JPL).

$NE\Delta T$, which is the temperature difference corresponding to the standard deviation of the radiance within a homogeneous, isothermal scene region. For TIR imagers such as ASTER, $NE\Delta T_{300K} \approx 0.25$ K. Also for ASTER, the $NE\Delta T$, atmospheric correction, and radiometric calibration all introduce errors of about the same size, leading to a total uncertainty in the recovered LST of about 1.5 K and in the LSE of ~ 0.015 .

Deterministic solutions for emissivity

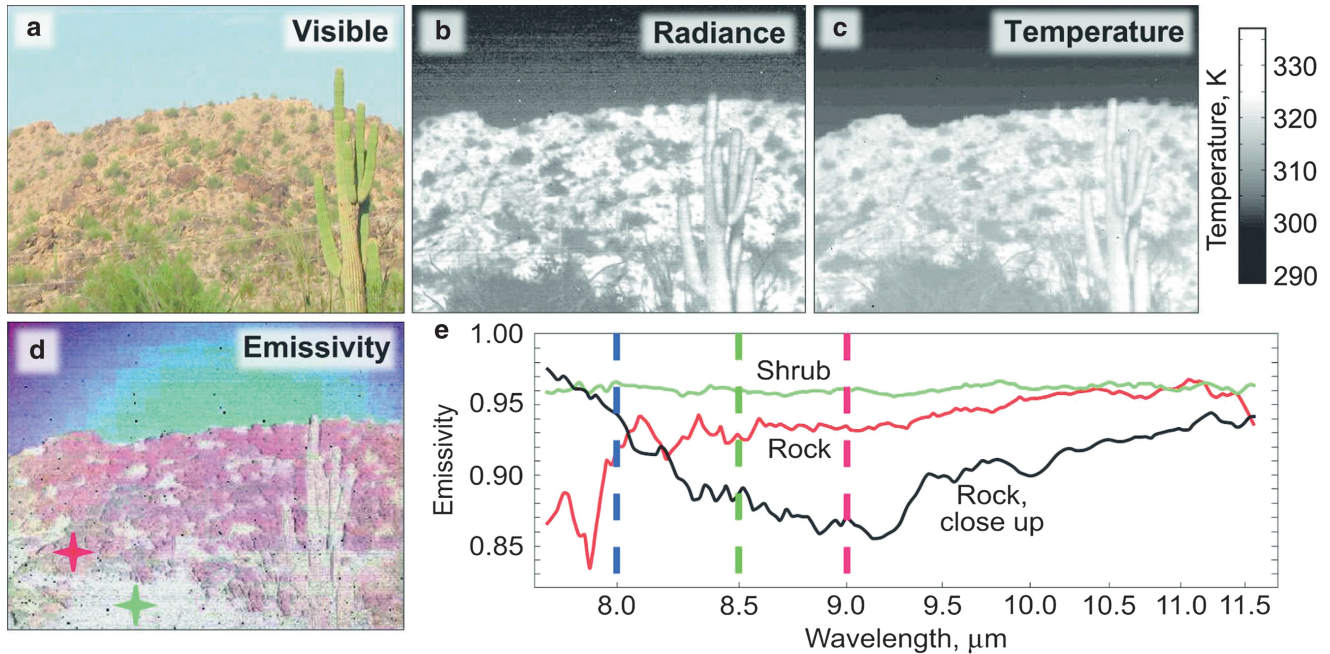
As discussed in *Land Surface Temperature*, recovering both LST and LSE from a single image is underdetermined. In principle, this problem can be removed by increasing the number of images acquired for the same scene. For each n -channel image, after atmospheric compensation, there are $n + 1$ unknowns, but only n measurements; for two images of the same scene, there are $n + 2$ unknowns, but $2n$ measurements (assuming LST has changed but LSE has remained constant). Therefore, a two-channel image taken at two different times is

deterministic. It is additionally necessary that the LST be significantly different between acquisitions.

Two-time, two-channel approach

If well-registered multispectral day–night radiance measurements are available, it is possible to determine T and ε uniquely (Watson, 1992a). Although this approach is esthetic, for most TIR data, the recovered temperatures and emissivities tend to be imprecise. For example, for image channels at 8 and 12 μm , day–night temperatures of 290 and 310 K, and for $NE\Delta T = 0.3$ K, recovered LST would have an uncertainty of ≥ 20 K. This arises because of the flat shape of the Planck curve in the spectral range around 300 K.

Wan (1999) showed that using an image channel in the 3–5 μm window, where the slope of the Planck function is steep, can improve the precision greatly and used the day–night algorithm to make a standard MODIS LST product. However, for daytime data, reflected sunlight at 3–5 μm must be accounted for (see *Land Surface Temperature*, Figure 3). Furthermore, acquiring data 12 h or more apart



Land Surface Emissivity, Figure 2 TIR images and spectra, South Mountain, Arizona, looking SE. (a) Natural color; (b) TIR radiance at 9 μm ; (c) brightness temperature; (d) emissivity (RGB = 8, 8.5 and 9 μm , respectively); (e) emissivity spectra measured with the TELOPS, Inc., FIRST hyperspectral imaging spectrometer, August 8, 2007. The shrub spectrum was taken from the site in d marked the green cross; the rock spectrum from the red cross. Differences in the “rock” spectra likely relate to differences in the pixel field of view and exact location, and in the length of the atmospheric path between the sample and sensor.

adds complexity because the scene may have changed between images, for example, because of dew.

It is also advantageous to use more than two channels, in which case the inversion for LST and LSE is overdetermined. This has the advantage of reducing the impact of measurement errors. The exaggeration of measurement error in this otherwise esthetic technique will become less severe as high-precision imagers such as SEBASS ($NE\Delta T_{300K, 11\mu m} < 0.05$ K: Hackwell et al., 1996) become widely available.

Emissivity bounds method

Jaggi et al. (1992) observed that for every pixel and every channel i there exists a locus of (T, ϵ_i) vectors that are possible solutions for the modified Planck equation (Equation 1, *Land Surface Temperature*). Because T must be the same for all image channels, some (T, ϵ_i) pairs can be ruled out as candidate solutions. The range of solutions is even more limited if ϵ and/or T can be restricted a priori. For the land surface, it is commonly possible to assume that $0.8 < \epsilon < 1.0$, for example.

This elegant approach is not truly deterministic, because it requires assumed limits to ϵ and/or T . However, it requires no empirical assumptions. The technique does not appear to have been widely used, perhaps because it does not identify the most probable values of ϵ or T , only possible ranges. In practice, performance depends on

how well emissivity limits are known a priori, and implementation would probably require some sort of image classification to establish them closely.

Spectral-shape solutions

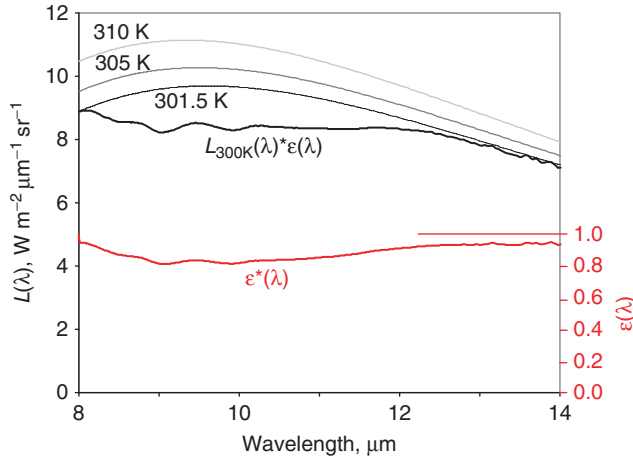
Although it is not possible to invert the modified Planck equation for both ϵ and T without external constraints, it is possible to estimate spectral shape for ϵ , at the expense of T and of the amplitude of the recovered spectrum, that is, the recovered spectra are essentially normalized, so that only relative amplitudes (wavelength to wavelength) are known. This is nevertheless useful, since composition is generally determined from spectral shape, and not the absolute amplitudes.

Ratio methods

Watson (1992b) observed that ratios of spectrally adjacent channels i and j described spectral shape accurately, provided that T could be estimated even roughly:

$$\frac{\epsilon_j}{\epsilon_i} = \frac{L_j \lambda_i^5 (\exp(c_2/(\lambda_i T)) - 1)}{L_i \lambda_j^5 (\exp(c_2/(\lambda_j T)) - 1)} \quad (2)$$

(c_2 is a constant from Planck’s law, Equation 1, *Land Surface Temperature*). To calculate the ϵ ratios, it is necessary first to approximate the temperature T from the measured radiances L_i and L_j . If ϵ can be estimated



Land Surface Emissivity, Figure 3 Emissivity $\varepsilon(\lambda)$ and spectral radiance spectra $L(\lambda)$ for basalt at 300 K. $L(\lambda)$ was calculated as the product of measured $\varepsilon(\lambda)$ and a 300 K blackbody ($B(\lambda)$) spectrum. In “Planck draping,” blackbody spectra are calculated for successively lower temperatures (e.g., 310, 305 and 301.5 K, above) until $\varepsilon_{max} B(\lambda) = L(\lambda)$ at some wavelength. The maximum emissivity, ε_{max} must be estimated, usually as a value near 0.95 as in the example shown. $\varepsilon^*(\lambda)$, the recovered $\varepsilon(\lambda)$, is calculated as $L(\lambda)/B(\lambda)$. Both it and the found LST (301.5 K, above) will be inaccurate unless the Planck functions are scaled correctly by ε_{max} . In the example shown, LST is in error by 1.5 K. The error warps $\varepsilon^*(\lambda)$ slightly.

within ± 0.075 , the uncertainty in T is ± 5 K, and the ε ratios can be estimated with an average error of ~ 0.007 (this estimate does not include the effects of measurement error).

Becker and Li (1990) proposed a similar approach they called the “temperature-independent spectral indices” (TISI) method. TISI begins with the observation (Slater, 1980) that Planck’s law may be represented by

$$B_k(T_s) = \alpha_k(T_o) T^{n_k(T_o)} \quad (3)$$

where B is the spectral radiance in image channel k for a blackbody at temperature T_s and T_o is a reference temperature. Constants n_k and α_k are given by

$$n_k(T_o) = \frac{c_2}{\lambda_k T_o} \left(1 + \frac{1}{\exp(c_2/\lambda_k T_o) - 1} \right); \quad (4)$$

$$\alpha_k(T_o) = \frac{B_k(T_o)}{T_o^{n_k(T_o)}}$$

(Dash, 2005). The land-leaving spectral radiance L_k , corrected for atmospheric absorption and path radiance but not down-welling spectral irradiance L_k^\downarrow , is thus

$$L_k = \varepsilon_k \alpha_k T_s^{n_k} C_k; \quad C_k = 1 + \frac{(1 - \varepsilon_k) L_k^\downarrow}{\varepsilon_k B_k(T_s)} \quad (5)$$

where C_k is spatially variable and atmosphere specific. The TISI is found by rationing spectral radiances for image channels i and j :

$$\frac{L_i^{a_i}}{L_j^{a_j}} = \frac{\varepsilon_i^{a_i} \alpha_i^{a_i} T_s^{n_i a_i} C_i^{a_i}}{\varepsilon_j^{a_j} \alpha_j^{a_j} T_s^{n_j a_j} C_j^{a_j}} \quad (6)$$

Here a_i is defined as n_i^{-1} (and $a_j = n_j^{-1}$), chosen to make Equation 6 independent of T . Since for a wide range of temperatures the C ratio is close to unity, TISI is then

$$TISI_{i,j} = \left[\frac{L_i}{\alpha_i} \right]^{1/n_i} \left[\frac{L_j}{\alpha_j} \right]^{-1/n_j} = \frac{\varepsilon_i^{1/n_i} C_i^{1/n_i}}{\varepsilon_j^{1/n_j} C_j^{1/n_j}} \approx \frac{\varepsilon_i^{1/n_i}}{\varepsilon_j^{1/n_j}} \quad (7)$$

The ratio spectra are insensitive to temperature, for normal terrestrial ranges. The approaches are adaptable for most sensors.

Alpha-residual method

The alpha-residual algorithm produces a relative emissivity spectrum that preserves spectral shape but, like the ratio methods, does not yield actual ε or T values. The alpha residuals are calculated utilizing Wien’s approximation of Planck’s law, which neglects the “ -1 ” term in the denominator. This makes it possible to linearize the approximation with logarithms, thereby separating λ and T :

$$\frac{c_2}{T} \approx \lambda_j \ln(\varepsilon_j) - \lambda_j \ln(L_j) + \lambda_j \ln(c_1) - 5\lambda_j \ln(\lambda_j) - \lambda_j \ln(\pi). \quad (8)$$

Here c_1 and c_2 are the constants defined in Planck’s law (Equation 1, *Land Surface Temperature*) and j is the image channel. Wien’s approximation introduces a systematic error in ε_j of $\sim 1\%$ at 300 K and 10 μm wavelength.

The next step is to calculate the means for the parameters of the linearized equation, summing over the n image channels:

$$\frac{c_2}{T} \approx \frac{1}{n} \sum_{j=1}^n \lambda_j \ln(\varepsilon_j) - \frac{5}{n} \sum_{j=1}^n \lambda_j \ln(\lambda_j) - \frac{1}{n} \sum_{j=1}^n \lambda_j \ln(L_j) + (\ln(c_1) - \ln(\pi)) \frac{1}{n} \sum_{j=1}^n \lambda_j. \quad (9)$$

The residual is calculated by subtracting the mean from the individual channel values. Collecting terms, a set of n equations is generated relating ε_i to L_i , independent of T :

$$\lambda_j \ln(\varepsilon_j) - \mu_\varepsilon = \lambda_j \ln(\lambda_j) - \frac{1}{n} \sum_{j=1}^n \lambda_j \ln(L_j) + \kappa_i. \quad (10a)$$

$$\kappa_i \approx 5\lambda_i \ln(\lambda_i) - \sum_{j=1}^n \lambda_j \ln(\lambda_j) - (\ln(c_1) - \ln(\pi))(\lambda_j - \bar{\lambda}) \quad (10b)$$

$$\mu_\alpha = \frac{1}{n} \sum_{j=1}^n \lambda_j \ln(\varepsilon_j); \quad \bar{\lambda} = \frac{1}{n} \sum_{j=1}^n \lambda_j \quad (10c)$$

Note that κ_i contains only terms which do not include the measured spectral radiances, L_i , and hence may be calculated from the constants. Although dependency on T has been eliminated, it has been replaced by the unknown μ_α , related to the mean emissivity, such that the total number of unknowns is unchanged. The components of the alpha-residual spectrum vary only with the measured radiances. They are defined as

$$\alpha_i \equiv \lambda_i \ln(\varepsilon_i) - \mu_\alpha \quad (11)$$

and are equivalent to the right-hand side of Equation 10a (α is defined differently than in the TISI method).

Model approaches

In this section, three algorithms distinguished by their model assumptions are described. The most specific requires that both a value of ε and the wavelength at which it occurs be known. The next requires only that the value be known. The third does not require the value of the emissivity to be known, only that the emissivity at two known wavelengths be the same.

The model emissivity (or reference channel) method (Kahle et al., 1980) assumes that the value of ε for one of the image channel's *ref* is constant and known a priori, reducing the number of unknowns to the number of measurements. First, the temperature is estimated using

$$T = \frac{c_2}{\lambda_{ref}} \left(\ln \left(\frac{c_1 \varepsilon_{ref}}{\pi L_{ref} \lambda_{ref}^5} \right) + 1 \right)^{-1} \quad (12)$$

Lyon (1965) suggested that, for most rocks, the maximum emissivity (ε_{max}) was commonly ~ 0.95 and occurred at the long-wavelength end of the 8–14 μm TIR window. This observation has been used to justify the assumption $\varepsilon_{ref} = \varepsilon_{max}$, typically for $10 < \lambda_{ref} < 12 \mu\text{m}$.

Blackbody spectral radiances B_j for the remainder of the channels are next calculated from T and Planck's law. The model emissivities are $\varepsilon_j = L_j/B_j$.

No single value of ε_{ref} is appropriate for all surfaces. For example, for vegetation, $\varepsilon_{max} \approx 0.983$; if the value is assumed to be 0.95, the emissivities will be underestimated, the spectrum warped, and T overestimated by ~ 2.3 K. Vegetation, snow, and water are all subject to this kind of error. Also, reststrahlen bands for some types of rocks, for example, peridotite, occur near 10 μm , and ε_{max} occurs at shorter wavelengths. For these rock types, the errors may be even greater. Nevertheless, the model emissivity approach is robust and has the virtue of simplicity. It produces reliable results for a wide range of surface materials.

Retaining the assumption $\varepsilon_{ref} = \varepsilon_{max}$ but allowing the reference channel to vary, pixel by pixel, allows the model emissivity approach to be accurate for a wider range of materials. This approach is called the normalized emissivity method (NEM) (Gillespie, 1985; Realmuto, 1990). First, the brightness temperature T_b is found for each image channel, using Planck's law. T_b differs from channel to channel only if ε_j does also, since the actual skin temperature must be the same. The channel j with the maximum T_b is also the channel for which the maximum ε_j occurs and becomes the reference channel. For 81 spectra evaluated by Hook et al. (1992), 58 % of the temperatures found by the NEM algorithm were accurate to within 1 K, compared to only 21 % of temperatures recovered using the model emissivity method.

Finding the maximum T_b has been called the "Planck draping" method (Figure 3). This approach has been used to estimate $\varepsilon(\lambda)$ from high-resolution radiance spectra collected by hyperspectral imagers such as SEBASS or by field spectrometers.

Instead of examining the same scene element at two different times and temperatures, as in the day–night method, the scene element may be measured at different wavelengths λ_i and λ_j , chosen such that $\varepsilon_i = \varepsilon_j$. In such a case, it is necessary to find T (the "color temperature," T_c ; see Equations 10 and 11, *Land Surface Temperature*) and only a single ε for the two channels, and the situation is deterministic (two measurements, L_i and L_j , and the two unknowns, T_c and $\varepsilon_i = \varepsilon_j$). As for the reference channel method, T_c can then be used to calculate a blackbody spectrum B , from which $\varepsilon(\lambda)$ can be found. This treatment has been called the "graybody emissivity method" (Barducci and Pippi, 1996).

The strength of the technique lies in its ability to recover emissivities even if the value of ε is unknown. The main weaknesses are that for imagers with only a few TIR channels, the basic requirement, $\varepsilon_i = \varepsilon_j$, is not met for much of the land surface, and it is not always possible to know λ_i and λ_j . If the assumption is valid, the accuracy for T is comparable to NEM, provided λ_i and λ_j are widely separated (e.g., Mushkin et al., 2005), but for most rock spectra, errors are ≥ 5 K. Barducci and Pippi (1996) proposed the graybody emissivity method for hyperspectral scanners, for which the basic requirement is more likely to be met.

Scaling approaches

Once relative spectra have been calculated, they can be calibrated to "absolute" emissivity provided a scaling factor is known. Applied to the ratio approach of Watson (1992b) or the TISI approach of Becker and Li (1990), this is basically the same as one of the model algorithms. However, scaling can also be done from empirical regression relating the shape of the emissivity spectrum to an absolute value at one wavelength. The regression is typically based on laboratory spectra of common scene components. More complex approaches also are possible: the first example given below combines the "two-channel,

two-time,” and TISI approaches to convert the relative TISI spectra to emissivities.

The hybrid TISI approaches requires first that daytime and nighttime MIR and LWIR images be acquired and co-registered and that their TISI ratios be calculated. Essentially, there are four measurements ($L_{MIR,day}$, $L_{LWIR,day}$, $L_{MIR,night}$, and $L_{LWIR,night}$), four unknowns (ε_{MIR} , ε_{LWIR}), and one model assumption (the solar irradiance on the target). The MIR reflectivity is the complement of ε_{MIR} by Kirchhoff's law (for the complete mathematical development, see Dash, 2005). Using widely separated image channels improves the precision of T and ε recovery (e.g., Mushkin et al., 2005).

Alpha-derived emissivity (ADE) method

The ADE method (Kealy and Gabell, 1990; Hook et al., 1992; Kealy and Hook, 1993) is based on the alpha-residual approach. To recover ε_i , μ_α may be estimated via an empirical regression to the variance parameter v_α found for laboratory spectra:

$$v_\alpha = \frac{1}{n-1} \sum_{j=1}^n \alpha_j^2 \quad (13)$$

where α is defined in Equation 11. The best-fitting curves relating μ_α and v_α are of the form $\mu_\alpha = cv_\alpha^{1/x}$, where c and x are empirically determined coefficients ($c = -0.085$, $v_\alpha = 0.40$, and $r^2 = 0.935$ for ASTER).

Once the emissivities have been estimated, the temperature may be calculated using Planck's law. For 95 % of the library spectra, T was recovered within 1.6 K of the correct value, and Hook et al. (1992) showed that 67 % were accurate to within 1 K, compared to 58 % for the NEM.

The key innovation of the ADE approach is to utilize the empirical relationship between the average ε and a measure of the spectral contrast or complexity in order to restore the amplitude to the alpha-residual spectrum. The regression is based on the observation that, for a blackbody, the mean emissivity is unity and the spectral variance is zero. For minerals with reststrahlen bands or other emissivity features, the variance is greater than zero and, of course, the mean is less than unity. In use, the mean is predicted from the variance, which is calculated from the measured radiances.

Temperature–emissivity separation algorithm (TES)

The TES algorithm (Gillespie et al., 1998) uses a variant of the “minimum–maximum difference” or MMD approach of Matsunaga (1994) to scale relative emissivity spectra. TES is used to generate standard T and ε products from ASTER, but it has been generalized for different scanners. TES can work with as few as three channels provided the channel wavelengths are well chosen to capture the range of emissivities in scene spectra.

The MMD algorithm is related to the ADE algorithm, but is simpler. Whereas ADE utilizes the empirical

relationship between the mean emissivity $\bar{\varepsilon}$ and the variance of alpha-residual emissivities, MMD utilizes an assumed linear relationship between $\bar{\varepsilon}$ and the range of the emissivities themselves, represented by the maximum–minimum difference or *MMD*.

The MMD algorithm requires that the ε spectrum be estimated (e.g., using NEM) in order to calculate *MMD*, from which $\bar{\varepsilon}$ is predicted. The apparent spectrum is then rescaled according to this average, T is calculated, and the process is iterated until the change in T is less than the *NEAT*.

TES uses land-leaving spectral radiance and downwelling sky irradiance as input and provides a first guess for T and ε_j using the NEM algorithm. The correction for reflected sky irradiance is

$$L'_j = L_j - \frac{(1 - \varepsilon_j)}{\pi} I_\downarrow \quad (14)$$

where L_j is the ground-leaving spectral radiance, compensated for atmospheric absorption and path radiance, I_\downarrow is the downwelling sky irradiance, and $(1 - \varepsilon_j)$ is the scene reflectivity (Kirchhoff's law). The NEM emissivities are then recalculated from L'_j and normalized:

$$\beta_j = \frac{\varepsilon_j}{\bar{\varepsilon}} \quad (15)$$

MMD is calculated from the β spectrum and used to predict ε_{min} (instead of $\bar{\varepsilon}$, as in the MMD approach), which is used for scaling:

$$\varepsilon_{min} = 0.994 - 0.687 MMD^{0.737}; \quad \varepsilon_j = \beta_j \left(\frac{\varepsilon_{min}}{\beta_{min}} \right) \quad (16)$$

After early 2009, a linear regression ($\varepsilon_{min} = 0.8625MMD + 0.955$) was used for scaling in TES (Gustafson et al., 2006) in order to improve TES precision for low-contrast spectra in standard ASTER data products. The TES algorithm differs from the MMD approach in using a better estimate of the emissivity and in basing the “absolute” measure of emissivity on ε_{min} rather than $\bar{\varepsilon}$, a difference that results in less scatter of the data about the regressed line and, hence, improved performance (± 1.5 K; ± 0.015 ε).

Classification-based algorithms

Classification approaches exploit the relationship between composition and ε and/or ρ to estimate ε pixel by pixel in at least one-image channel, generally in order to find T . T can then be used to calculate $\varepsilon(\lambda)$ in the other channels. Approaches that use channels in reflected sunlight (0.4–2.5 μm) require imagers with multiple, co-registered telescopes. They also make the assumption that TIR emissivities and visible–SWIR reflectivities are correlated. In some cases, for example, vegetation or water, the TIR emissivities can be predicted accurately; in others, for

example, many rocks, this assumption is less robust. Nevertheless, simply being able to distinguish rock and/or soil from vegetation can improve accuracy by 1–2 K. As an example, the NDVI approach (see Equation 9, *Land Surface Temperature*) makes use of co-registered visible red ($\sim 0.65 \mu\text{m}$) and near-infrared (NIR: $0.7\text{--}1.2 \mu\text{m}$) daytime image channels in order to recognize pixels that have a significant fraction of vegetation.

Conclusions

Only a fraction of published temperature–emissivity separation algorithms have been discussed here. (For an alternative summary, see Dash (2005).) Increasingly sophisticated approaches are being devised to improve on old treatments, for example, by using neural net technology to tune algorithms (e.g., Mao et al., 2008; Liang, 1997). However, the basic categories discussed above still apply.

For the most part, calibration inaccuracies, measurement uncertainty, and inaccurate atmospheric characterization all contribute to errors in the recovered LST and LSE. These errors are commonly as large as or larger than those attributable to the algorithms themselves, at least for the high-resolution imagers commonly used for Earth-surface studies. Therefore, algorithms themselves are now not the dominant factor limiting recovery accuracy. However, the next few years may see the introduction of a new generation of sensors, such as SEBASS, with dramatically improved measurement characteristics. In this case, atmospheric compensation may become the biggest source of uncertainty and deserving of attention. Likewise, the performance of some algorithms like the “two-time, two-channel” algorithm that now are strongly limited by measurement precision may improve relative to those algorithms that are limited by different factors, such as TES with its empirical regression of ϵ_{min} and *MMD*.

Bibliography

- Barducci, A., and Pippi, I., 1996. Temperature and emissivity retrieval from remotely sensed images using the “grey body emissivity” method. *IEEE Transactions on Geoscience and Remote Sensing*, **34**(3), 681–695.
- Becker, F., and Li, Z. L., 1990. Temperature-independent spectral indices in thermal infrared bands. *Remote Sensing of Environment*, **32**, 17–33.
- Clark, R. N., Swayze, G. A., Livo, K. E., Kokaly, R. F., Sutley, S. J., Dalton, J. B., McDougal, R. R., and Gent, C. A., 2003. Imaging spectroscopy: earth and planetary remote sensing with the USGS Tetracorder and expert systems. *Journal of Geophysical Research*, doi:10.1029/2002JE001847.
- Dash, P., 2005. *Land Surface Temperature and Emissivity Retrieval from satellite Measurements*. Dissertation, Forschungszentrum Karlsruhe in der Helmholtz-Gemeinschaft, Wissenschaftliche Berichte, FZKA 7095, 99 pp. Available from <http://bibliothek.fzk.de/zb/berichte/FZKA7095.pdf>. Last Accessed July 7, 2013.
- Gillespie, A. R., 1985. Lithologic mapping of silicate rocks using TIMS. In *The TIMS Data Users' Workshop*, June 18–19, Jet Propulsion Laboratory Publication 86–38. Pasadena, CA: Jet Propulsion Lab, pp. 29–44.
- Gillespie, A. R., Kahle, A. B., and Walker, R. E., 1986. Color enhancement of highly correlated images I. Decorrelation and HSI contrast stretches. *Remote Sensing of Environment*, **20**, 209–235.
- Gillespie, A. R., Matsunaga, T., Rokugawa, S., and Hook, S. J., 1998. Temperature and emissivity separation from advanced spaceborne thermal emission and reflection radiometer (ASTER) images. *IEEE Transactions on Geoscience and Remote Sensing*, **36**, 1113–1126.
- Gustafson, W. T., Gillespie, A. R., and Yamada, G., 2006. Revisions to the ASTER temperature/emissivity separation algorithm. In Sobrino, J. A. (ed.), *Second Recent Advances in Quantitative Remote Sensing*. Spain: Publicacions de la Universitat de València, pp. 770–775, ISBN 84-370-6533-X; 978-84-370-6533-5.
- Hackwell, J. A., Warren, D. W., Bongiovi, R. P., Hansel, S. J., Hayhurst, T. L., Mabry, D. J., Sivjee, M. G., and Skinner, J. W., 1996. LWIR/MWIR imaging hyperspectral sensor for airborne and ground-based remote sensing. *Proceedings-SPIE The International Society For Optical Engineering*, **2819**, 102–107.
- Hook, S. J., Gabell, A. R., Green, A. A., and Kealy, P. S., 1992. A comparison of techniques for extracting emissivity information from thermal infrared data for geologic studies. *Remote Sensing of Environment*, **42**, 123–135.
- Hunt, G., 1980. Electromagnetic radiation: the communication link in remote sensing. In Siegal, B. S., and Gillespie, A. R. (eds.), *Remote Sensing in Geology*. New York: Wiley, pp. 5–45.
- Jaggi, S., Quattrochi, D., and Baskin, R., 1992. An algorithm for the estimation of bounds on the emissivity and temperatures from thermal multispectral airborne remotely sensed data (Abstract). In Realmuto, V. J. (ed.), *Summary of the Third Annual JPL Airborne Geoscience Workshop*, June 1–5, Jet Propulsion Laboratory Publication 92–14. Pasadena, CA: Jet Propulsion Lab, pp. 22–24.
- Kahle, A. B., and Rowan, L. C., 1980. Evaluation of multispectral middle infrared aircraft images for lithological mapping in the east Tintic Mountains, Utah. *Geology*, **8**, 234–239.
- Kahle, A. B., Madura, D. P., and Soha, J. M., 1980. Middle infrared multispectral aircraft scanner data: analysis for geological applications. *Applied Optics*, **19**, 2279–2290.
- Kealy, P. S., and Gabell, A. R., 1990. Estimation of emissivity and temperature using alpha coefficients. In *Proceedings of the 2nd TIMS Workshop*, Jet Propulsion Laboratory Publication 90–55. Pasadena, CA: Jet Propulsion Lab, pp. 11–15.
- Kealy, P. S., and Hook, S. J., 1993. Separating temperature and emissivity in thermal infrared multispectral scanner data: implication for recovering land surface temperatures. *IEEE Transactions on Geoscience and Remote Sensing*, **31**(6), 1155–1164.
- Liang, S. L., 1997. Retrieval of land surface temperature and water vapor content from AVHRR thermal imagery using artificial neural network. *International Geoscience and Remote Sensing Symposium Proceedings*, **3**, 1959–1961.
- Lyon, R. J. P., 1965. Analysis of rocks by spectral infrared emission (8 to 25 microns). *Economic Geology*, **60**, 715–736.
- Mao, K., Shi, J., Tang, H., Li, Z.-L., Wang, X., and Chen, K.-S., 2008. A neural network technique for separating land surface emissivity and temperature from ASTER imagery. *IEEE Transactions on Geoscience and Remote Sensing*, **46**(1), 200–208.
- Matsunaga, T., 1994. A temperature-emissivity separation method using an empirical relationship between the mean, the maximum, and the minimum of the thermal infrared emissivity spectrum. *Journal of the Remote Sensing Society of Japan*, **14**(2), 230–241 (in Japanese with English abstract).
- Mushkin, A., Balick, L. K., and Gillespie, A. R., 2005. Extending surface temperature and emissivity retrieval to the mid-infrared (3–5 μm) using the Multispectral Thermal Imager (MTI). *Remote Sensing of Environment*, **98**, 141–151.

- Norman, J. M., and Becker, F., 1995. Terminology in thermal infrared remote sensing of natural surfaces. *Remote Sensing Reviews*, **12**, 159–173.
- Palluconi, F. D., and Meeks, G. R., 1985. *Thermal Infrared Multi-spectral Scanner (TIMS): An Investigator's Guide to TIMS Data*. Jet Propulsion Laboratory Publication 85–32. Pasadena, CA: Jet Propulsion Lab, 14 pp.
- Realmutto, V. J., 1990. Separating the effects of temperature and emissivity: emissivity spectrum normalization. In *Proceedings of the 2nd TIMS Workshop*, Jet Propulsion Laboratory Publication 90–55. Pasadena, CA: Jet Propulsion Lab, pp. 31–36.
- Salisbury, J. W., and D'Aria, D., 1992. Emissivity of terrestrial materials in the 8–14 μm atmospheric window. *Remote Sensing of Environment*, **42**, 83–106.
- Slater, P. N., 1980. *Remote Sensing, Optics and Optical Systems*. Reading, MA: Addison-Wesley, p. 575.
- Soha, J. M., and Schwartz, A. A., 1978. Multispectral histogram normalization contrast enhancement. In *Proceedings of the 5th Canadian Symposium on Remote Sensing*, Victoria, British Columbia, Canada, pp. 86–93.
- Wan, Z., 1999. MODIS land-surface temperature algorithm theoretical basis document (LST ATBD), Version 3.3. *NASA Contract NAS5-31370*, 37 pp.
- Watson, K., 1992a. Two-temperature method for measuring emissivity. *Remote Sensing of Environment*, **42**, 117–121.
- Watson, K., 1992b. Spectral ratio method for measuring emissivity. *Remote Sensing of Environment*, **42**, 113–116.

Cross-references

Crop Stress
 Fields and Radiation
 Land Surface Temperature
 Optical/Infrared, Radiative Transfer
 Volcanism

LAND SURFACE ROUGHNESS

Thomas Farr
 Jet Propulsion Laboratory, California Institute of
 Technology, Pasadena, CA, USA

Synonyms

Microrelief; Microtopography

Definition

Surface roughness is usually defined at the human scales of centimeter to a few meter; larger scales are usually considered as topography. Relief at these scales is familiar to field geologists working at the outcrop scale and those interested in interpretation of landforms and earth-surface processes that form and modify them.

Scientific usefulness

One important surficial geologic process is aeolian erosion, transport, and deposition of sediments. The shear stress wind produces at the earth's surface is strongly affected by the surface roughness. The aerodynamic roughness

parameter, z_0 , depends on the wind speed profile as a function of height about the ground (Greeley et al., 1997). This parameter is used by geologists interested in aeolian processes as well as climatologists seeking to quantify atmospheric coupling with the solid earth.

Windblown dust and sand can also modify surface roughness by mantling and attenuating surface roughness (Farr, 1992; Arvidson et al., 1993). This can lead to estimates of relative age for surfaces such as lava flows or alluvial fans exposed to the same rate of aeolian deposition (Farr, 1992; Farr and Chadwick, 1996).

Streambed and ocean-bottom roughness also affect the flow and transport capabilities of water in those environments (e.g., Butler et al., 2001).

Other geologic processes produce or modify surface roughness, in particular volcanic eruptions which may mantle surfaces with ash or produce new roughness elements through extrusion of lava flows which can be relatively smooth pahoehoe or extremely rough aa. Roughness of lava flows can provide information on their eruption characteristics, such as rate and temperature (e.g., Lescinsky et al., 2007).

Land surface roughness strongly affects many remote sensing techniques. Observations of reflected visible-near-infrared wavelengths are affected by sub-resolution self-shadowing of roughness elements. Thus, rougher surfaces are darker, and the shadows are illuminated by sky light or reflections from adjacent land, shifting the spectral signature of the surface (Adams and Gillespie, 2006). At thermal infrared and microwave wavelengths, which are dominated by emission from solar-heated surfaces, roughness as well as larger-scale topography affects the initial heating of the surface while roughness also affects the efficiency of emission (Ulaby et al., 1982). Active microwave (radar) systems image surfaces through scattering of a transmitted wave from the surface. Smooth surfaces at the scale of the wavelengths, which are typically centimeter-meter, reflect energy away from the receiving antenna and are imaged as dark surfaces, while rough surfaces scatter the incident energy in all directions and show up in bright tones on radar images (Henderson and Lewis, 1998).

Much work has gone into quantitative models which seek to remove the effects of roughness on sub-resolution shadowing and thermal heating and emission (Tsang et al., 2000; Adams and Gillespie, 2006). In the radar area, inversion models have been developed which estimate the surface roughness from radar observations at different angles, polarizations, and wavelengths (Ulaby et al., 1982; Van Zyl et al., 1991; Evans et al., 1992; Dubois et al., 1995; Tsang et al., 2000).

Quantifying surface roughness

Good reviews of techniques for describing quantitatively surface roughness can be found in Dierking (1999), Thomas (1999), Shepard et al. (2001), and Campbell (2002), Chap. 3. The simplest description of surface



<http://www.springer.com/978-0-387-36698-2>

Encyclopedia of Remote Sensing

Njoku, E.G. (Ed.)

2014, XXV, 939 p. 370 illus., 223 illus. in color.,

Hardcover

ISBN: 978-0-387-36698-2